

Embedded magnetic phases in (Ga,Fe)N: the key role of growth temperature

A. Navarro-Quezada,¹ W. Stefanowicz,^{2,3} Tian Li,¹ B. Faina,¹ M. Rovezzi,^{1,4} R. T. Lechner,¹
T. Devillers,¹ F. d'Acapito,^{4,5} G. Bauer,¹ M. Sawicki,³ T. Dietl,^{3,6} and A. Bonanni¹

¹*Institut für Halbleiter-und-Festkörperphysik, Johannes Kepler University, Altenbergerstr. 69, A-4040 Linz, Austria**

²*Laboratory of Magnetism, Białystok University, ul. Lipowa 41, 15-424 Białystok, Poland*

³*Institute of Physics, Polish Academy of Sciences,
al. Lotników 32/46, PL-02-668 Warszawa, Poland*

⁴*Italian Collaborating Research Group, BM08 "GILDA" - ESRF, BP 220, F-38043 Grenoble, France*

⁵*CNR-IOM Sez. di Grenoble, c/o ESRF 6, Rue Jules Horowitz, F-38043 Grenoble (France)*

⁶*Institute of Theoretical Physics, University of Warsaw, PL-00-681 Warszawa, Poland*

(Dated: February 4, 2022)

The local chemistry, structure, and magnetism of (Ga,Fe)N nanocomposites grown by metal organic vapor phase epitaxy is studied by high resolution synchrotron x-ray diffraction and absorption, transmission electron microscopy, and superconducting quantum interference device magnetometry as a function of the growth temperature T_g . Three contributions to the magnetization are identified: i) paramagnetic – originating from dilute and non-interacting Fe^{3+} ions substitutional of Ga, and dominating in layers obtained at the lowest considered T_g (800°C); ii) superparamagnetic-like – brought about mainly by ferromagnetic nanocrystals of $\varepsilon\text{-Fe}_3\text{N}$ but also by $\gamma\text{-Fe}_4\text{N}$ and by inclusions of elemental $\alpha\text{-Fe}$ and $\gamma\text{-Fe}$, and prevalent in films obtained in the intermediate T_g range; iii) component linear in the magnetic field and associated with antiferromagnetic interactions – found to originate from highly nitridated Fe_xN ($x \leq 2$) phases, like $\zeta\text{-Fe}_2\text{N}$, and detected in samples deposited at the highest employed temperature, $T_g = 950^\circ\text{C}$. Furthermore, depending on T_g , the Fe-rich nanocrystals segregate towards the sample surface or occupy two-dimensional planes perpendicular to the growth direction.

PACS numbers: 68.55.Nq, 75.50.Pp, 75.75.-c, 81.05.Ea

I. INTRODUCTION

The epitaxy of magnetically doped semiconductors constitutes a versatile mean of fabricating in a self-organized way semiconductor/ferromagnet nanocomposites¹⁻³ with still widely unexplored but remarkable functionalities relevant to spintronics, nanoelectronics, photonics, and plasmonics. In these nanocomposite materials the presence of robust ferromagnetism correlates with the existence of nanoscale volumes containing a large density of magnetic cations, that is with the formation of condensed magnetic semiconductors (CMSs) buried in the host matrix and characterized by a high spin ordering temperature.⁴ The aggregation of CMSs and, therefore, the ferromagnetism of the resulting composite system shows a dramatic dependence on the growth conditions and co-doping with shallow impurities.

In particular, the understanding and control of CMSs in tetrahedrally coordinated semiconductor films containing transition metals (TMs) – typical examples being (Ga,Mn)As,⁵ (Ga,Mn)N,⁶ (Ge,Mn),⁷ (Zn,Cr)Te,⁸ and (Ga,Fe)N⁹⁻¹¹ – have been lately carefully considered with the necessary aid of nanoscale characterization techniques. Indeed, the control over the CMSs formation as a function of the fabrication parameters, and the possibility to reliably produce on demand CMSs with a pre-defined size, structure, and distribution in the semiconductor host, are fundamental requisites for the exploitation of these nanostructures in functional devices. At the same time these studies draw us nearer to understand the

origin of the ferromagnetic-like features – persisting up to above room temperature (RT) – found in a number of semiconductors and oxides.^{12,13}

Dilute zincblende (Ga,Mn)As grown by molecular beam epitaxy (MBE) is known to decompose upon annealing with the formation of embedded MnAs nanocrystals coherent with the GaAs matrix,¹⁴ and a striking spin-battery effect produced by these CMSs has been already proven.¹⁵ As an example of the critical role played by growth parameters, MBE $\text{Ge}_{1-x}\text{Mn}_x$ grown below 130°C is seen to promote the self-assembling of coherent magnetic Mn-rich nanocolumns whilst a higher growth temperature leads to the formation of hexagonal Ge_5Mn_3 nanocrystals buried in the Ge host.¹⁶

Following theoretical suggestions,¹⁷ it has recently been demonstrated experimentally that it is possible to change the charge state of TM ions in a semiconducting matrix and, therefore, the aggregation energy by co-doping with shallow donors or acceptors.^{8,10} In particular, it has been proven that in the model case of wurtzite (wz) (Ga,Fe)N fabricated by metalorganic vapor phase epitaxy (MOVPE) the Fermi-level tuning by co-doping with Mg (acceptor in GaN) or Si (donor in GaN) is instrumental in controlling the magnetic ions aggregation.¹⁰

The same system has been thoroughly analyzed at the nanoscale by means of advanced electron microscopy as well as by synchrotron-based diffraction and absorption techniques. The structural characteristics have then been related – together with the growth parameters – to the magnetic properties of the material as evidenced by

superconducting quantum interference device (SQUID) magnetometry.^{9–11} It has been concluded that for a concentration of Fe below its optimized solubility limit ($\sim 0.4\%$ of the magnetic ions) the dilute system is predominantly paramagnetic (PM). For higher concentrations of the magnetic ions (Ga,Fe)N shows either chemical- (intermediate state) or crystallographic-phase separation.^{9–11} In the phase-separated layers a ferromagnetic (FM) behavior persisting far above RT is observed, and has been related to the presence of either Fe-rich regions coherent with the host GaN (in the intermediate state) or of Fe_xN nanocrystals in the GaN matrix. These investigations appear to elucidate the microscopic origin of the magnetic behavior of (Ga,Fe)N reported by other groups.^{18,19}

Along the above mentioned lines, in this work we consider further the MOVPE (Ga,Fe)N material system and we reconstruct the phase diagram of the Fe_xN nanocrystals buried in GaN as a function of the growth temperature. Synchrotron radiation x-ray diffraction (SXRD), extended fine structure x-ray absorption (EXAFS) and x-ray absorption near-edge fine structure (XANES), combined with high-resolution transmission electron microscopy (HRTEM) and SQUID magnetometry allow us to detect and to identify particular Fe_xN phases in samples fabricated at different growth temperatures T_g as well as to establish a correlation between the existence of the specific phases and the magnetic response of the system. Our results imply, in particular, that self-assembled nanocrystals with a high concentration of the magnetic constituent account for ferromagnetic-like features persisting up to above RT. These findings for (Ga,Fe)N do not support, therefore, the recent suggestions that high temperature ferromagnetism of – the closely related – oxides is brought about by spin polarization of defects, whereas the role of magnetic impurities is to bring the Fermi energy to an appropriate position in the band gap.¹³

We find that already a 5% variation in the growth temperature is critical for the onset of new Fe_xN species and we can confirm that an increase in the growth temperature promotes the aggregation of the magnetic ions, resulting in an enhanced density of Fe-rich nanocrystals in the matrix and in a consequent increase of the ferromagnetic response of the system. Moreover, we observe that while in the low-range of growth temperatures the Fe-rich nanoobjects tend to segregate close to the sample surface, at higher T_g two-dimensional assemblies of nanocrystals form in a reproducible way at different depths in the layer, an arrangement expected to have a potential as template for the self-aggregation of metallic nanocolumns.²⁰ The non-uniform distribution of magnetic aggregates over the film volume here revealed, implies also that the CMS detection may be challenging and, in general, requires a careful examination of the whole layer, including the surface and interfacial regions.

The paper is organized as follows: in the next Section we give a concise summary of the MOVPE process employed to fabricate the (Ga,Fe)N phase-separated sam-

ples together with a brief description of the characterization techniques. A table with the relevant samples and relative parameters completes this part. The central results of this work are reported in Section III and are presented in two sub-sections discussing respectively: i) the detection, identification and structural properties *vs.* T_g of the different Fe_xN nanocrystals in phase-separated (Ga,Fe)N, with the distribution of the nanocrystals in the sample volume, and ii) the magnetic properties of the specific families of Fe_xN phases. In Section IV we sum up the main conclusions and the prospects of this work.

II. EXPERIMENTAL PROCEDURE

A. Growth of (Ga,Fe)N

We summarize here our study by considering a series of wurtzite (Ga,Fe)N samples fabricated by MOVPE in an AIXTRON 200 RF horizontal reactor. All structures have been deposited on *c*-plane sapphire substrates with TMGa (trimethylgallium), NH_3 , and FeCp_2 (ferrocene) as precursors for, respectively, Ga, N and Fe, and with H_2 as carrier gas.

The growth process has been carried out according to a well established procedure,²¹ namely: substrate nitridation, low temperature (540°C) deposition of a GaN nucleation layer (NL), annealing of the NL under NH_3 until recrystallization and the growth of a $\approx 1\ \mu\text{m}$ thick device-quality GaN buffer at 1030°C . On the GaN buffer, Fe-doped GaN overlayers ($\approx 700\ \text{nm}$ thick) have been deposited at different T_g ranging from 800°C to 950°C , with a V/III ratio of 300 [NH_3 and TMGa source flow of 1500 standard cubic centimeters per minute (sccm) and 5 sccm, respectively], with an average growth-rate of $0.21\ \text{nm/s}$, and the flow-rate of the Fe-precursor set at 300 sccm. During the whole growth process the samples have been continuously rotated in order to promote the deposition homogeneity, while *in situ* and on line ellipsometry is employed for the real time control over the entire fabrication process.

The considered samples main parameters, including the Fe concentration, are displayed in Table I.

B. Synchrotron x-ray diffraction – experimental

Coplanar SXRD measurements have been carried out at the Rossendorf Beamline BM20 of the European Synchrotron Radiation Facility (ESRF) in Grenoble – France, using a photon energy of $10.005\ \text{keV}$. The x-ray data correspond to the diffracted intensities in reciprocal space along the sample surface normals. The beamline is equipped with a double-crystal Si(111) monochromator with two collimating/focusing mirrors (Si and Pt-coating) for rejection of higher harmonics, allowing measurements in an energy range of 6 to 33 keV. The sym-

TABLE I: Considered (Ga,Fe)N samples with the corresponding growth temperature, Fe concentration as evaluated by secondary ions mass spectroscopy (SIMS) as well as concentration of the dilute paramagnetic Fe^{3+} ions $x_{\text{Fe}^{3+}}$ and a lower limit of the concentration of Fe ions x_{Fe_N} contributing to the Fe-rich nanocrystals, as obtained from magnetization data.

Sample	T_g °C	Fe concentration [10^{20} cm^{-3}]	$x_{\text{Fe}^{3+}}$ [10^{19} cm^{-3}]	x_{Fe_N} [10^{19} cm^{-3}]
S690	800	1	3.2	0.1
S687	850	2	2.9	1.7
S680	850	2	2.7	1.5
S987	900	4	2.4	1.6
S691	950	4	2.9	3.2

metric $\omega = 2\theta$ scans are acquired using a heavy-duty 6-circle Huber diffractometer and the most intense peaks are found for 2θ up to 40° .

C. XAFS – experimental and method

X-ray absorption fine structure (XAFS) measurements at the Fe K edge (7112 eV) are carried out at the “GILDA” Italian collaborating research group beamline²² (BM08) of ESRF under the same experimental conditions reported in Ref. 11, collecting both the XANES and EXAFS spectra, and employing the following method for the analysis.

A set of model compounds is established: Fe substitutional of Ga in GaN (Fe_{Ga}),¹¹ ζ - Fe_2N ,²³ ϵ - Fe_3N ,²⁴ γ - Fe_4N ,²⁴ α -Fe²⁵ and γ -Fe.²⁶ For these input structures the XANES absorption spectra are calculated using the FDMNES code²⁷ while the EXAFS scattering expansion signals are computed with the FEFF8.4 code²⁸ in order to de-correlate the structural results to a specific software choice. In both cases muffin-tin potentials and the Hedin-Lunqvist approximation for their energy-dependent part is used, with self-consistent potential calculation for enhancing the accuracy in the determination of the Fermi energy (E_F).

X-ray polarization is taken into account for Fe_{Ga} while unpolarized simulations are conducted for the other phases assuming a random orientation of the nanocrystals in the sample. In addition, for XANES the convergence of the results is tested against the increasing in the input cluster size (>150 atoms) and the method is validated by experimental values from Fe_{Ga} and α -Fe. The resulting simulated spectra are then convoluted *via* an energy-dependent function as implemented in FDMNES²⁷ plus a Gaussian experimental broadening of 1 eV and fitted to the normalized XANES experimental data in the energy range from -20 to 80 eV relative to E_F with a linear combination analysis using the ATHENA graphical interface²⁹ to IFEFFIT.³⁰

All the possible combinations with a maximum of three

spectra per fit (maximum of six fit parameters: amplitude and energy shift) are tested and the best fit is chosen on the basis of the χ^2 statistics, discarding unphysical results. Finally, the XANES results are independently checked through the quantitative analysis of the EXAFS data where the background-subtracted (via the VIPER program³¹) k^2 -weighted fine-structure oscillations, $\chi(k)$, are fitted in the Fourier-transformed space.

D. High resolution transmission electron microscopy – experimental

The HRTEM studies are performed on cross-sectional samples prepared by standard mechanical polishing followed by Ar^+ ion milling at 4 kV for about 1 h. Conventional diffraction contrast images in bright-field imaging mode and high-resolution phase contrast pictures were obtained from a JEOL 2011 Fast TEM microscope operating at 200 kV and capable of an ultimate point-to-point resolution of 0.19 nm and allowing to image lattice fringes with a 0.14 nm resolution.

Additionally, energy dispersive x-ray (EDS) analysis has been performed *via* an Oxford Inca EDS equipped with a silicon detector to obtain information on the local composition. Selected area electron diffraction (SAED) and fast Fourier transform (FFT) procedures are employed to study scattering orders and d -spacing for respectively the larger and the smaller nanocrystals.

E. SQUID magnetometry – experimental

The magnetic properties have been investigated in a Quantum Design MPMS XL 5 SQUID magnetometer between 1.85 and 400 K and up to 50 kOe following the methodology described previously.³²

The difference between the magnetization values measured up to 50 kOe at 1.8 K and 5 K is employed to determine the concentration $x_{\text{Fe}^{3+}}$ of paramagnetic Fe^{3+} ions in the layers.³³ The lower limit of the concentration of Fe ions contributing to the Fe-rich nanocrystals, as well as an assessment of their Curie temperature is inferred from magnetization curves at higher temperatures.

Finally, measurements of field cooled (FC) and zero field cooled (ZFC) magnetization hint to the influence of the growth temperature on the size distribution of the nanocrystals.

III. RESULTS

A. Fe_xN phases *vs.* T_g in crystallographically separated (Ga,Fe)N

Before entering into the detailed discussion of our studies, we would like to point out that the reproducibility of the data has been accurately tested and: i) different

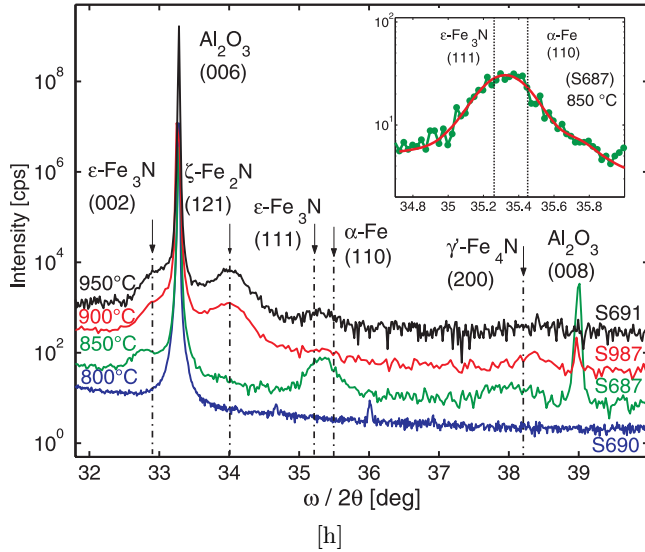


FIG. 1: (Color online) SXR D spectra for (Ga,Fe)N layers deposited at different growth temperatures. Inset: peak at 35.3° deconvoluted into two components assigned to diffraction maxima (111) of ϵ -Fe₃N and (110) of α -Fe [experiment (dotted line) and fit (smooth line)].

samples grown under the same conditions have been characterized, ii) all measurements (SXR D, HRTEM, etc...) have been repeated in different runs on the same samples and we can conclude that both the (Ga,Fe)N structures are stable over time and the formation of different phases is reproduced when the growth conditions are fidely replicated.

In Fig. 1 we report SXR D diffraction spectra for the (Ga,Fe)N samples grown at different temperatures, as listed in Table I. For the layer S690 fabricated at 800°C we have no evidence of secondary phases and only diffraction peaks originating from the sapphire substrate and from the GaN matrix are revealed, in agreement with HRTEM measurements showing no phase separation. Moreover, in order to test the stability of the dilute phase, we have annealed the samples up to $T_a = 900^\circ\text{C}$ and *in situ* SXR D measurements upon annealing do not reveal the onset of any secondary phases, as reported in Fig. 2, in accord with the behavior of dilute Mn in GaN³² and in contrast with (Ga,Mn)As where post-growth annealing is found to promote the precipitation of MnAs nanocrystals.⁵

Moving to a T_g of 850°C (S687) different diffraction peaks belonging to secondary phases become evident. We have previously reported⁹ that when growing (Ga,Fe)N at this temperature, one dominant Fe-rich phase is formed, namely wurzite ϵ -Fe₃N, for which we identify two main peaks corresponding to the (002) and the (111) reflexes, respectively. A closer inspection of the (111)-related feature and a fit with two gaussian curves centered at 35.2° and 35.4° , gives evidence of the presence of the (110) reflex from cubic metallic α -Fe. Moreover, the broad feature appearing around 38° is associated to

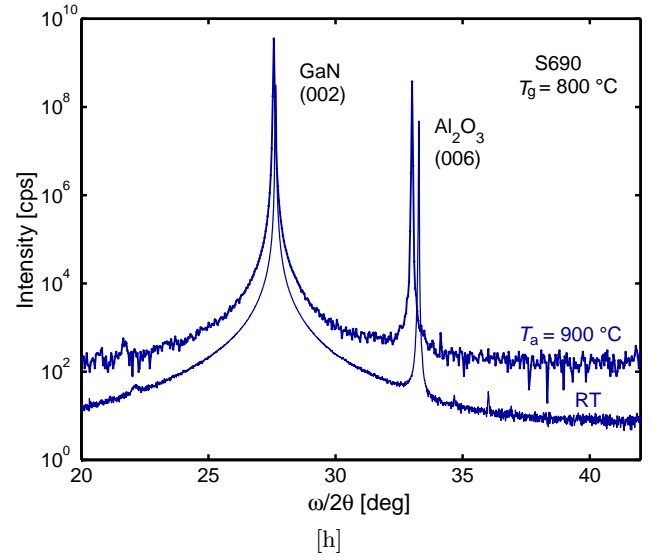


FIG. 2: SXR D spectra for a dilute (Ga,Fe)N sample (S690) as grown and upon *in situ* annealing at $T_a = 900^\circ\text{C}$ for 1 h, indicating that post-growth annealing does not induce - in the SXR D sensitivity range - crystallographic decomposition.

the (200) reflex of face centered cubic (*fcc*) γ -Fe₄N, that crystallizes in an inverse perovskite structure.³⁴ From the position of the peak, we can estimate that these nanocrystals are strained.

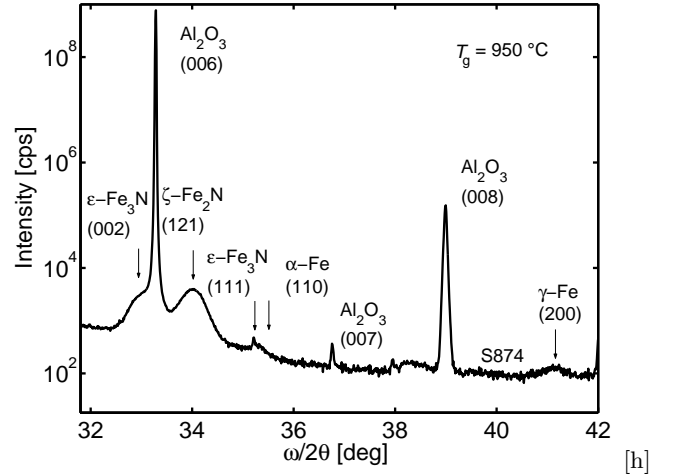


FIG. 3: SXR D for a sample (S874) grown at 950°C evidencing the aggregation of (200) γ -Fe in the (Ga,Fe)N layer.

As the growth temperature is increased to 900°C (S987) there is no contribution left from the (110) α -Fe phase, and the signal from the (111) of ϵ -Fe₃N is significantly quenched, indicating the reduction in either size or density of the specific phase. Furthermore, an intense peak is seen at 34° , corresponding to the (121) contribution from orthorhombic ζ -Fe₂N. This phase crystallizes in the α -PbO₂-like structure, where the Fe atoms show a slightly distorted hexagonal close packing (*hcp*), also

found for ε -Fe₃N.²⁴

The structural resemblance of ε -Fe₃N and the ζ -Fe₂N is remarkable, as the *hcp* arrangement in ε -Fe₃N is nearly retained in ζ -Fe₂N.²³ This gives a hint of the likely direct conversion of phase from ε -Fe₃N into ζ -Fe₂N. The diffraction peak from (200) γ' -Fe₄N is still present at this temperature, but its position is slightly shifted to its bulk value. A similar behavior is observed for the diffraction from (200) ε -Fe₃N (002), shifted from 32.78° to 32.9°.

At a growth temperature of 950°C (S691) the diffraction peak of (200) γ' -Fe₄N recedes, indicating the decomposition of this *fcc* phase at temperatures above 900°C, in agreement with the phase diagram for free standing Fe_xN,²⁴ reporting cubic γ' -Fe₄N as stable at low temperatures. Only the (002) ε -Fe₃N- and the (121) ζ -Fe₂N-related diffraction peaks are preserved with a constant intensity and position with increasing temperature, suggesting that at high T_g these two phases and their corresponding orientations, are noticeably stable. Furthermore, in samples grown at this T_g the peak from (200) γ -Fe is detected around 41.12°, as reported in Fig. 3, in agreement with the XAFS data discussed later in this Section.

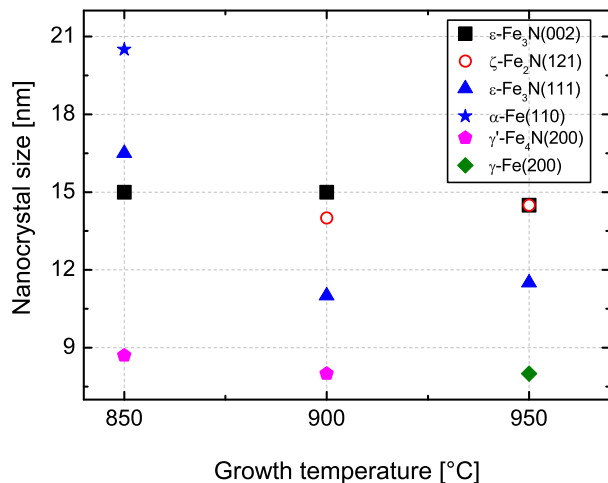


FIG. 4: (Color online) Average size *vs.* T_g of nanocrystals in the different Fe_xN phases, as determined from SXRD.

Following the procedure employed previously,³⁵ and based on the Williamson-Hall formula method,³⁶ we obtain the approximate average nanocrystals size from the full-width at half maximum (FWHM) of the diffraction peaks in the radial ($\omega/2\theta$) scans. The FWHM of the (002) ε -Fe₃N, of the (200) γ' -Fe₄N, and of the (121) ζ -Fe₂N diffraction peaks are comparable for samples grown at different temperatures, indicating that the average size of the corresponding nanocrystals is also constant, as summarized in Fig. 4.

The (111) ε -Fe₃N signal intensity is seen to change

abruptly when comparing the results for the sample grown at 850°C to those from the layers fabricated at higher temperatures. From the FWHM for this particular orientation we can estimate that the nanocrystal average size adjusts between 16.5 and 12.0 nm in the considered temperature range. At high temperatures, the size then remains constant up to 950°C. The size of the α -Fe nanocrystals can only be estimated for the sample grown at 850°C, where the corresponding diffraction peak can easily be resolved and suggests an average size of these objects larger than that of the other identified phases, as confirmed by the HRTEM images reported in Fig. 6.

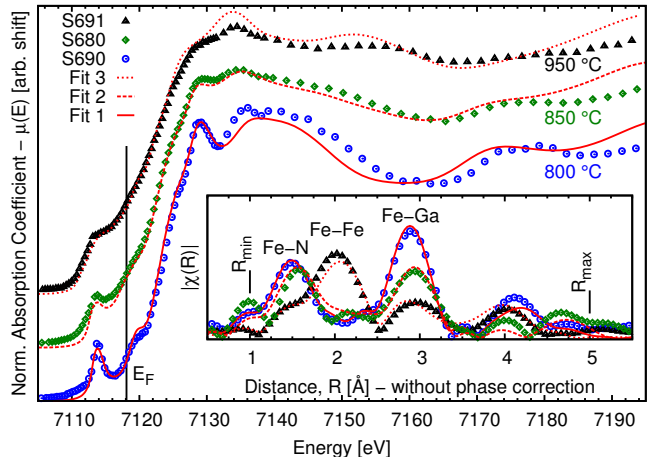


FIG. 5: (Color online) Normalized XANES spectra (main plot) and the amplitude of the Fourier-transforms (inset) of the k^2 -weighted EXAFS in the range from 2.5 to 10.0 Å⁻¹ for three samples (points) grown at different temperatures, with their relative fits (lines) summarized in Table II.

The XAFS study on the (Ga,Fe)N samples fabricated at different T_g permits to have a structural description of the atomic environment around the absorbing species from a local point of view, complementary to SXRD. The experimental data are reported in Fig. 5 with the relative fits obtained by following the method described in Sec. II C. Qualitatively an evolution with T_g is visible and it is quantitatively confirmed by the results summarized in Table II.

In particular, from the XANES analysis – sensitive to the occupation site symmetry and multiple scattering effects – it is possible to infer how the composition of the different phases evolves with increasing T_g : Fe_{Ga} reduces, while ε -Fe₃N increases up to 950°C when the precipitation is in favor of ζ -Fe₂N and γ -Fe. This behavior is confirmed also by the EXAFS spectra given in the inset to Fig. 5, where the first three main peaks in the fit range from R_{\min} to R_{\max} represent, respectively, the average Fe-N, Fe-Fe and Fe-Ga coordination.

In addition, the signal present at longer distances confirms the high crystallinity and permits to include important multiple scattering paths in the fits for a better identification of the correct phase. In fact, from the Fe-

Fe distances it is possible to distinguish Fe_xN (≈ 2.75 Å) from pure Fe phases (≈ 2.57 Å), while the distinction between α -Fe and γ -Fe is possible with the different multiple scattering paths generated from the body centered cubic (*bcc*) and from the *fcc* structure, respectively.

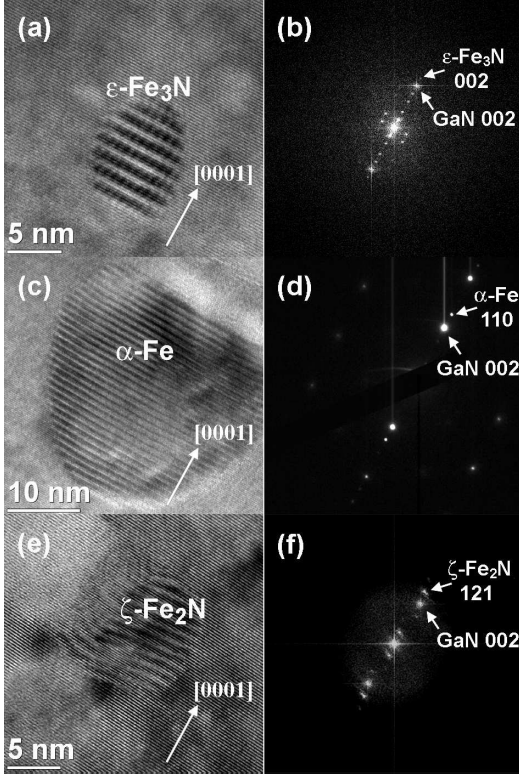


FIG. 6: Transmission electron micrographs of different Fe_xN phases: (a) HRTEM image of a $\epsilon\text{-Fe}_3\text{N}$ nanocrystal; (b) the corresponding FFT image, revealing that the d -spacing along the growth direction is about 0.216 nm. (c) HRTEM image on $\alpha\text{-Fe}$ nanocrystal in sample S687; (d) SAED pattern on the enclosing area. (e) HRTEM image of a $\zeta\text{-Fe}_2\text{N}$ nanocrystal; (f) the corresponding FFT image, revealing that the d -spacing along the growth direction is about 0.211 nm.

The presence of the different Fe_xN phases detected with SXRD has been confirmed also by HRTEM measurements on the considered samples, as reported in Fig. 6. All the HRTEM images presented here have been taken along the $[10\bar{1}0]$ zone axis.

By using the SAED technique for the larger nanocrystals and a FFT combined with a subsequent reconstruction for the smaller objects, we have studied the foreign scattering orders and the d -spacings along the growth direction. As shown in Fig. 6(a), the transitional Moiré fringes indicate that there is a set of planes parallel to the GaN (002) ones with a similar d -spacing inside the nanocrystal. The corresponding FFT image shown in Fig. 6(b) gives an additional diffraction spot close to GaN (002), corresponding to a d -spacing of 0.217 nm, matching the d_{002} of $\epsilon\text{-Fe}_3\text{N}$. The $\epsilon\text{-Fe}_3\text{N}$ phase is found in all the considered samples, with the exception of the

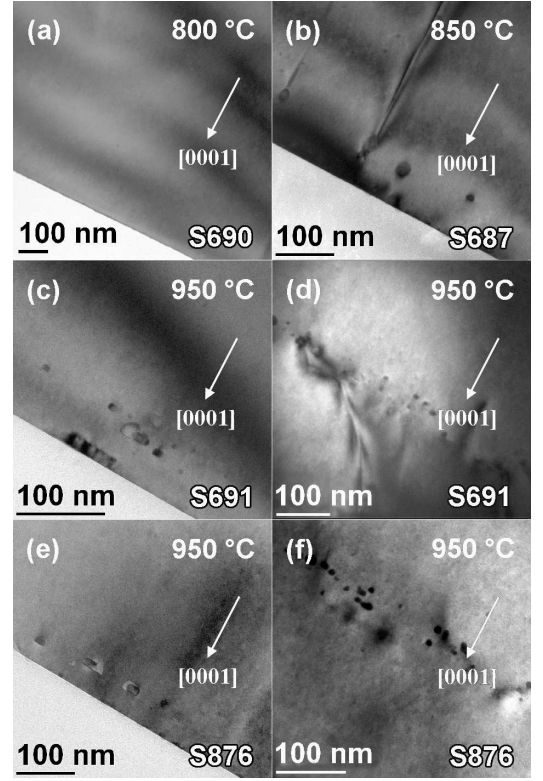


FIG. 7: (Color online) TEM images: distribution of the Fe-rich nanocrystals with increasing growth temperature. (a) $T_g = 800^\circ\text{C}$ (S690) – dilute (Ga,Fe)N; (b) $T_g = 850^\circ\text{C}$ (S687), Fe-rich nanocrystals concentrated in proximity of the samples interface solely; $T_g = 950^\circ\text{C}$ (S691) – Fe-rich nanocrystals segregating in proximity of the sample surface (c) and of the interface between the GaN buffer and the Fe-doped layer (d); (e),(f) $T_g = 950^\circ\text{C}$ (S876) – to be compared with the TEM images of S691 in (c) and (d): reproducibility in the distribution of the Fe-rich nanocrystals for different samples grown at the same T_g .

one grown at 800°C (S690, dilute). The phase $\epsilon\text{-Fe}_3\text{N}$ has the closest structure to wurtzite GaN and we can assume that the formation of $\epsilon\text{-Fe}_3\text{N}$ is, thus, energetically favored.³⁷

The micrograph displayed in Fig. 6(c) has been obtained from the layer grown at 850°C and refers to a nanocrystal located in the proximity of the sample surface. The corresponding SAED pattern in Fig. 6(d) reveals that the d -spacing of the lattice planes overlapping the GaN matrix has a value of 0.203 nm, matching the d_{110} of $\alpha\text{-Fe}$. For values of T_g between 900 and 950°C , nanocrystals like the one represented in Fig. 6(e) are found. The FFT image shown in Fig. 6(f), reveals that the additional d -spacing is 0.211 nm, corresponding to the d_{121} of $\zeta\text{-Fe}_2\text{N}$.

It should be underlined here that the size of the nanocrystals in the HRTEM images is smaller than the average value obtained from SXRD. This discrepancy originates from the fact that a cross-sectional TEM spec-

TABLE II: Quantitative results of the XAFS analysis (best fits). XANES: composition (x) and energy shift relative to E_F (ΔE) for each structure; EXAFS: average distance (R) and Debye-Waller factor (σ^2) for the first three coordination shells around the absorber. For each phase the coordination numbers are kept to the crystallographic ones and rescaled by the relative fractions found by XANES and a global amplitude reduction factor, S_0^2 , of 0.93(5) as found for Fe_{Ga} . Error bars on the last digit are reported in parentheses.

Fit	XANES								EXAFS					
	Fe_{Ga}		$\zeta\text{-Fe}_2\text{N}$		$\varepsilon\text{-Fe}_3\text{N}$		$\gamma\text{-Fe}$		Fe-N		Fe-Fe		Fe-Ga	
	x	ΔE (eV)	x	ΔE (eV)	x	ΔE (eV)	x	ΔE (eV)	R (Å)	σ^2 (10^{-3}Å^2)	R (Å)	σ^2 (10^{-3}Å^2)	R (Å)	σ^2 (10^{-3}Å^2)
1	0.9(1)	1.3(5)	-	-	0.1(1)	2.9(9)	-	-	1.99(1)	5(2)	2.75(5)	13(5)	3.20(1)	7(1)
2	0.6(1)	1.1(5)	-	-	0.4(1)	1.8(5)	-	-	2.00(2)	4(1)	2.76(2)	9(4)	3.20(1)	8(1)
3	0.2(1)	1.0(5)	0.4(1)	4.5(5)	-	-	0.4(1)	-0.3(5)	1.95(4)	10(9)	2.60(5)	15(9)	3.18(2)	4(2)

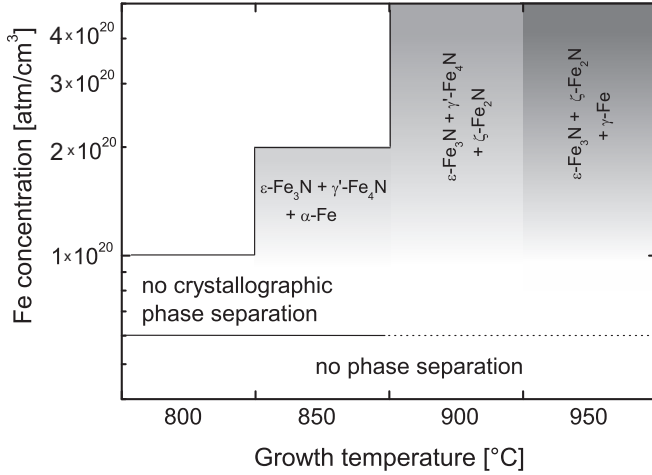


FIG. 8: A phase diagram of (Ga,Fe)N as a function of the growth temperature.

imen must be rendered considerably thin, in order to achieve a sufficient transparency to the electron beam. Therefore, a nanocrystal is usually only partly enclosed in the investigated area. At the same time, in low magnification micrographs on thicker volumes the size of the objects becomes comparable to the average value determined by the SXRD studies.

Cross-sectional low-magnification TEM measurements permit to observe that while at the lower growth temperatures the Fe-rich nanoobjects tend to segregate close to the sample surface as seen in Fig. 7(b), at higher T_g two-dimensional assemblies of nanocrystals form in a reproducible way – as proven by comparing Fig. 7(c),(d) and Fig. 7(e),(f) – and this arrangement is expected to be instrumental as template for the self-aggregation of metallic nanocolumns.²⁰

Summarizing the SXRD, XAFS and HRTEM findings, a phase diagram of the Fe-rich phases formed in (Ga,Fe)N as a function of the growth temperature is constructed and reported in Fig. 8, showing the dominant phases for each temperature interval.

According to Ref. 34 when the concentration of the

interstitial-atoms in the ε phase is increased by only 0.05 atoms/100 Fe, a phase transition from ε to ζ occurs. In this process the Fe atoms retain their relative positions but there is a slight anisotropic distortion of the ε lattice that reduces the symmetry of the (nano)crystal to ζ -orthorhombic. The hexagonal unit cell parameter a_{hex} of $\varepsilon\text{-Fe}_3\text{N}$ splits into the parameters b_{orth} and c_{orth} in $\zeta\text{-Fe}_2\text{N}$. Moreover, according to the Fe *vs.* N phase diagram the orthorhombic phase contains a higher percentage of nitrogen³⁴ compared to the hexagonal one, and this guides us to conjecture that the higher the growth temperature, the more nitrogen is introduced into the system.

Remarkable is the fact that by increasing the growth temperature the (002) $\varepsilon\text{-Fe}_3\text{N}$ is preserved, while the (111) oriented nanocrystals are not detected. A focused study would be necessary to clarify the kinetic processes taking place between 850°C and 900°C. Moreover, it is still to be clarified whether the fact that the $\varepsilon\text{-Fe}_3\text{N}$ nanocrystals oriented along the growth direction are stable, while the ones lying out of the growth plane are not, may be related to differences in surface energy.

The Fe_xN phases found in our (Ga,Fe)N samples are listed in Table III, together with their crystallographic structure, lattice parameters, d -spacing for the diffracted peaks, and magnetic properties.

Further focused studies are required in order to clarify the kinetic mechanisms of segregation and possibly the range of parameters that could allow the selectivity of the species in different two-dimensional regions of the doped layers.

B. Magnetic properties of Fe_xN phases

As reported in Table III, the different Fe_xN phases we identify in the considered samples are expected to show specific magnetic responses. The $\varepsilon\text{-Fe}_3\text{N}$ phase, predominant in the samples grown at 850°C, is ferromagnetic with a Curie temperature T_C of 575 K.⁴⁰

The $\gamma'\text{-Fe}_4\text{N}$ phase, also present though in lesser amount in these layers, is FM too, with a T_C of 750 K.³⁴

TABLE III: Structural and magnetic parameters of the Fe-rich phases found in the considered (Ga,Fe)N samples.

	Structure	Lattice parameter ³⁸			<i>d</i> -spacing			
		<i>a</i> (nm)	<i>b</i> (nm)	<i>c</i> (nm)	literature value ³⁹	SXRD	HRTEM	μ_B
γ' -Fe ₄ N	<i>fcc</i>	0.382	–	–	0.189	0.188-0.189	0.188	2.21 ³⁸
ε -Fe ₃ N	<i>wz</i>	0.469	–	0.438	0.2189 ₍₀₀₂₎	0.2188 ₍₀₀₂₎	0.2178 ₍₀₀₂₎	2.0 ⁴⁰
					0.208 ₍₁₁₁₎	0.206 ₍₁₁₁₎	–	
ζ -Fe ₂ N	<i>ortho</i>	0.443	0.554	0.484	0.2113	0.2114	0.211	1.5 ³⁸
α -Fe	<i>bcc</i>	0.286	–	–	0.202	0.204	0.203	2.2 ⁴¹
γ -Fe	<i>fcc</i>	0.361	–	–	0.180 ₍₂₀₀₎	0.176 ₍₂₀₀₎	–	0.3–1.6 ⁴²
					0.210 ₍₁₁₁₎	–	–	

For the samples deposited at temperatures above 850°C, the dominant and stable phase becomes ζ -Fe₂N.

The magnetic response of these (Ga,Fe)N layers is quite typical for semiconductors containing TM ions at concentration above or close to the solubility limits. Regardless of the prevailing diamagnetic component from the sapphire substrate – that we compensate with the procedure detailed elsewhere³² – the field dependency of magnetization $M(H)$ is characterized primarily by a dominant paramagnetic contribution at low temperatures from diluted substitutional Fe³⁺ ions and by a superparamagnetic-like component saturating (relatively) fast and originating from various magnetically ordered nanocrystals with high Fe content. Among them, the FM hexagonal ε -Fe_{3–*x*}N have the highest density, according to the SXRD and HRTEM studies discussed above. Despite the richness of different phases, it is relatively straightforward to separate these major components and to treat them – to a large extent – qualitatively.

We begin by noting that the superparamagnetic-like component originates primarily from nanocrystals characterized by a relatively high magnitude of the spin ordering temperature, so that their magnetization $M_N(T, H)$ can be regarded as temperature independent at very low temperatures. This means that a temperature dependence of the magnetization in this range comes from dilute Fe³⁺ ions, whose properties in GaN have been extensively investigated previously.^{33,43}

Accordingly, the concentration of these ions $x_{\text{Fe}^{3+}}$ can be obtained by fitting $g\mu_B S x_{\text{Fe}^{3+}} N_0 \Delta B_S(\Delta T, H)$ to the difference between the experimental values of the magnetization measured at 1.85 and 5.0 K, where $\Delta B_S(\Delta T, H)$ is the difference of the corresponding paramagnetic Brillouin functions $\Delta B_S(\Delta T, H) = B_S(1.85 \text{ K}, H) - B_S(5 \text{ K}, H)$. We consider the spin $S = 5/2$, the corresponding Landé factor $g = 2.0$, and treat $x_{\text{Fe}^{3+}}$ as the only fitting parameter.

The values established in this way are listed in Table I for the studied samples and they are then employed to calculate the paramagnetic contribution at any temperature according to $M = g\mu_B S x_{\text{Fe}^{3+}} B_S(T, H)$, which is then subtracted from the experimental data to obtain

the magnitude of the magnetization $M_N(T, H)$ coming from nanocrystals.

For the layers grown at $T_g < 900^\circ\text{C}$, $M_N(T, H)$ saturates at all investigated temperatures for a magnetic field above ~ 10 kOe, as evidenced in Fig. 9(a), pointing to a predominantly ferromagnetic order within the nanocrystals. The values of saturation magnetization M_N^{Sat} obtained in this way when plotted *vs.* temperature as in Fig. 9(b) allow us to assess the corresponding T_C from a fitting of the classical Brillouin function to the experimental points. Furthermore, assuming a value of the magnetic moment $2\mu_B$ per Fe, as in ε -Fe₃N,⁴⁴ we determine the concentration of Fe ions x_{Fe_N} contributing to the Fe-rich nanocrystals, as shown in Table I.

However, for the samples deposited at $T_g \geq 900^\circ\text{C}$ the magnitude of $M_N(H)$ saturates only at relatively high temperatures, namely around $T \gtrsim 150$ K, whereas at low temperatures it shows the sizable contribution of a slowly saturating component, as shown in Fig. 9(c) where magnetization data acquired at 1.85 K for the layer S691 are reported.

This new contribution must arise from magnetically coupled objects with a spin arrangement other than ferromagnetic. According to the SXRD measurements previously discussed and summarized in Fig. 1 the most likely candidate is orthorhombic ζ -Fe₂N, antiferromagnetic below 9 K,⁴⁵ or slowly saturating weakly ferromagnetic below 30 K.⁴⁶ In this case, in order to establish M_N^{Sat} we employ the Arrot plot method. The value of $M_N^{\text{Sat}}(T)$ determined in this way is reported in Fig. 9(d), and is seen to differ considerably from that of layers grown at lower T_g .

We are able to approximate the experimental values of $M_N^{\text{Sat}}(T)$ with a single Brillouin function only for $T \gtrsim 150$ K (dashed line in Fig. 9(d)). This points to a lower value of $T_C \cong 430$ K, indicating a shift of the chemical composition of ε -Fe_{3–*x*}N from Fe₃N ($x \cong 0$) for $T_g < 900^\circ\text{C}$ to at most Fe_{2.6}N ($x \cong 0.4$) for $T_g \geq 900^\circ\text{C}$, as T_C of ε -Fe_{3–*x*}N decreases with increasing nitrogen content.⁴⁴

Moreover, the gradually increasing values of $M_N^{\text{Sat}}(T)$ below $T \lesssim 150$ K, marked as the hatched area in Fig. 9(d), indicate the presence of even more diluted ε -

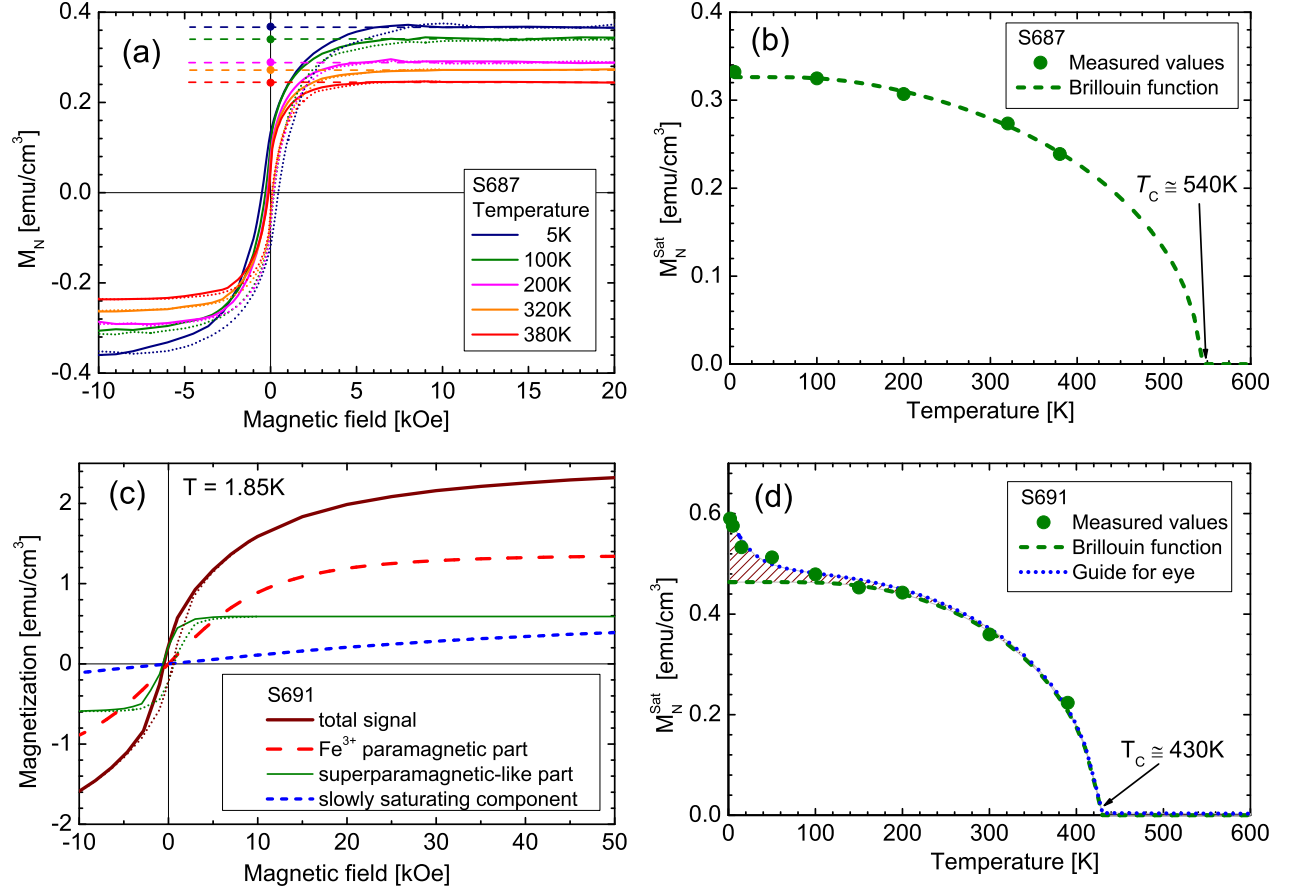


FIG. 9: (Color online) (a) Magnetic field dependence of the nanocrystals magnetization M_N at selected temperatures for sample S687 ($T_g = 850^\circ\text{C}$). Each $M_N(H)$ curve has been measured from the maximum positive to the maximum negative field, only and the dotted lines obtained by numerical inversion are guides for the eye. The dashed lines represent the saturation level of magnetization at each temperature. (b) Bullets - temperature dependence of the saturation magnetization M_N^{Sat} obtained from panel (a). Dashed line - the Brillouin function for the magnetic moment of $2\mu_B$ per Fe atom. (c) Three major contributions to the total magnetic signal (thick brown solid) for sample S691 ($T_g = 950^\circ\text{C}$): i) paramagnetic from Fe^{3+} (thick red dashed), ii) high- T_C superparamagnetic-like (thin green solid) from the nanocrystals and iii) slowly saturating component (blue short dashed). Also here only a half of the full hysteresis loop was measured and the dotted lines obtained by numerical reflection are guides for the eye. (d) Bullets - temperature dependence of M_N^{Sat} for sample S691. Dashed line - the Brillouin function for the magnetic moment of $2\mu_B$ per atom Fe. The blue dotted line follows the excess of M_N^{Sat} over the contribution from high T_C ferromagnetic nanocrystals.

Fe_{3-x}N nanocrystals with x ranging from 0.5 to 1 and with a wide spectrum of T_C . Importantly, since $\varepsilon\text{-Fe}_{3-x}\text{N}$ preserves its crystallographic structure and the changes of the lattice parameters are minor in the whole range $0 \leq x \leq 1$, all various $\varepsilon\text{-Fe}_{3-x}\text{N}$ nanocrystals contribute to the same diffraction peak in the SXRD spectrum, and are detected there as a single compound.

We note that the presence of either $\varepsilon\text{-Fe}_3\text{N}$ or $\zeta\text{-Fe}_2\text{N}$, characterized by a low spin ordering temperature, does not hinder the determination of the $x_{\text{Fe}^{3+}}$ values, as both compounds have a rather low magnetic moment of $0.1\mu_B$ per Fe atom. Accordingly, the resulting variation of their magnetization is small comparing to the changes of the Fe^{3+} paramagnetic signal at low temperatures.

The procedure exemplified above allows us to establish the lower limit for the Fe concentration that precipitates in the form of various Fe-rich nanocrystals (x_{Fe_N}), and that is determined by the magnitude of M_N^{Sat} at low temperatures. We again assume $2\mu_B$ per Fe atom, as in the dominant $\varepsilon\text{-Fe}_3\text{N}$. These values are collected in Table I and plotted as the function of T_g in Fig. 10. We see, that x_{Fe_N} consistently increases with T_g , and that the growth temperature plays a more crucial role than the Fe-precursor flow rate⁹ in establishing the total value of x_{Fe_N} .

Finally, measurements of FC and ZFC magnetization confirm the superparamagnetic-like behavior of $M_N(T, H)$, as reported in Fig. 11. As seen in Fig. 11(a),

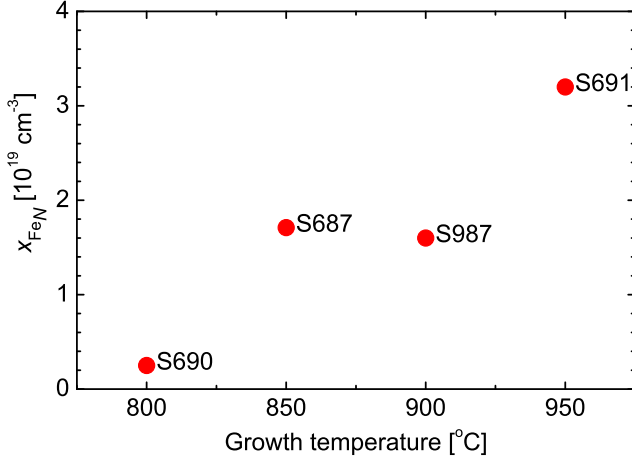


FIG. 10: (Color online) Estimated lower limit for the Fe concentration that precipitates in the form of various Fe-rich nanocrystals x_{FeN} as a function of the growth temperature.

the layer grown at the lowest temperature (S690) shows a minimal spread in T_B , having its maximum at $T_B < 100$ K, and accordingly a non-zero coercivity is evident only at low temperatures.

In contrast, for most of the studied layers a broad maximum on the ZFC curve, exemplified in Fig. 11(b), indicates a wide spread of blocking temperatures (T_B) – reaching RT – and consequently a broad distribution in the volume of the nanocrystals. These high values of T_B are responsible for the existence of the open hysteresis in the $M(H)$ curves seen in Figs. 9(a),(c) and thus of a non-zero coercivity. This observation again points to the growth temperature as to the key factor in the determination of the crystallographic structure, size and chemical composition of the Fe-rich nanocrystals.

IV. CONCLUSIONS

The previous^{9–11} and present studies allow us to draw a number of conclusions concerning the incorporation of Fe into GaN and about the resulting magnetic properties, expected to be generic for a broad class of magnetically doped semiconductors and oxides. These materials show magnetization consisting typically of two components: i) a paramagnetic contribution appearing at low temperatures and with characteristics typical for dilute magnetic semiconductors containing weakly interacting randomly distributed magnetic moments; ii) a puzzling ferromagnetic-like component persisting up to above RT but with a value of remanence much smaller than the magnitude of saturation magnetization.

According to SQUID and electron paramagnetic resonance⁹ measurements on (Ga,Fe)N, the concentration of Ga substituting the randomly distributed Fe^{3+} ions increases with the iron precursor flow rate reaching typi-

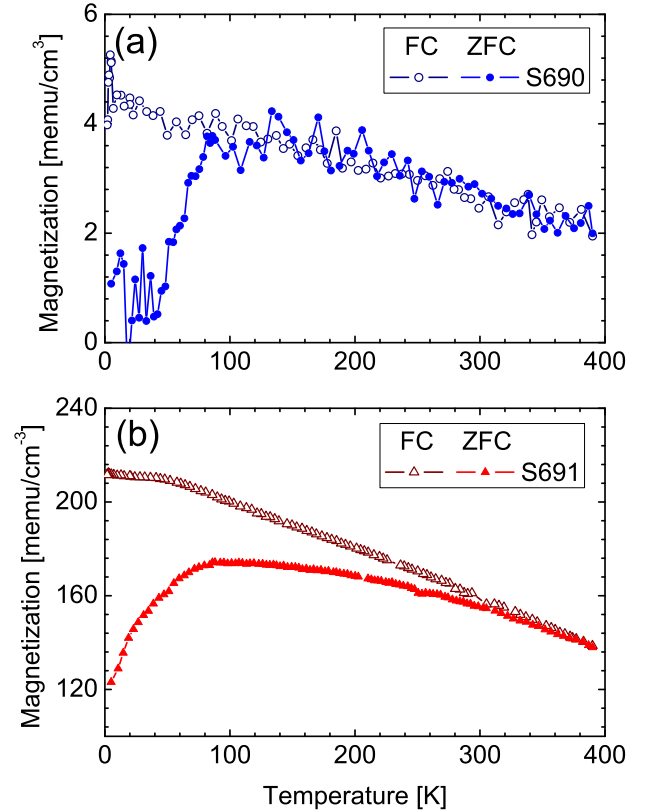


FIG. 11: (Color online) ZFC and FC curves measured in applied magnetic field of 200 Oe for samples grown at (a) 800°C and (b) 950°C.

cally the value of 0.1%. Our results imply that the magnitude of the paramagnetic response and, hence, the density of dilute Fe cations, does not virtually depend on the growth temperature. However, the incorporation of Fe can be enlarged by co-doping with Si donors, shifting the solubility limit to higher Fe concentrations.¹⁰

The presence of ferromagnetic-like features can be consistently interpreted in terms of crystallographic and/or chemical phase separations into nanoscale regions containing a large density of the magnetic constituent. Our extensive SQUID, SXRD, TEM, EXAFS, and XANES measurements of MOVPE-grown (Ga,Fe)N indicate that at the lowest growth temperature $T_g = 800^\circ\text{C}$, a large majority of the Fe ions occupy random Ga-substitutional positions. However, in films grown at higher temperatures, $850 \leq T_g \leq 950^\circ\text{C}$, a considerable variety of Fe-rich nanocrystals is formed, differing in the Fe to N ratio. In samples deposited at the low end of the T_g range, we observe mostly $\epsilon\text{-Fe}_3\text{N}$ precipitates but also inclusions of elemental α - and γ -Fe as well as of $\gamma'\text{-Fe}_4\text{N}$. In all these materials T_C is well above RT, so that the presence of the corresponding nanocrystals explains the robust superparamagnetic behavior of (Ga,Fe)N grown at $T_g \geq 850^\circ\text{C}$.

With the increase of the growth temperature nanocrystals of ζ -Fe₂N form and owing to antiferromagnetic interactions specific to this compound, the magnetization acquires a component linear in the magnetic field. This magnetic response has been previously observed and assigned to the Van Vleck paramagnetism of isolated Fe²⁺ ions. In view of the present findings, however, its interpretation in terms of antiferromagnetically coupled spins in nitrogen rich Fe_xN ($x \leq 2$) nanocrystals seems more grounded.

The total amount of Fe ions contributing to the formation of the Fe-rich nanocrystals is found to increase with the lowering of the growth rate and/or with the raising of the growth temperature. At the same time, however, the size of individual nanocrystals appears not to vary with the growth parameters. Furthermore, annealing of (Ga,Fe)N containing only diluted Fe cations does not result in a crystallographic phase separation. Altogether, our findings indicate that the aggregation of Fe ions occurs by nucleation at the growth front and is kinetically limited. Moreover, according to the TEM results presented here, the spatial distribution of nanocrystals is highly non-random. They tend to reside in two-

dimensional planes, particularly at the film surface and at the interface between the GaN buffer and the nominally Fe-doped layer.

As a whole, these findings constitute a significant step on the way to control the chemistry and local structure of semiconductor/ferromagnetic metal nanocomposites.

Acknowledgments

The work was supported by the European Research Council through the FunDMS Advanced Grant within the "Ideas" 7th Framework Programme of the EC, and by the Austrian Fonds zur Förderung der wissenschaftlichen Forschung – FWF (P18942, P20065 and N107-NAN). We acknowledge the technical staff at the Rossendorfer Beamline (BM20) of the ESRF, and in particular C. Bähz and N. Jeutter for their valuable assistance. We also thank R. Jakiela for performing SIMS measurements.

-
- * Electronic address: andrea.navarro-quezada@jku.at, alberta.bonanni@kylunet.nl, G. Biliyar, C. V. Hoof, and G. Borghs, App. Phys. Lett. **68**, 2744 (1996).
- ¹ A. Bonanni, Semicond. Sci. Technol. **22**, R41 (2007).
 - ² H. Katayama-Yoshida, K. Sato, T. Fukushima, M. Toyoda, H. Kizaki, V. Dinh, and P. Dederichs, phys. stat. sol. (a) **204**, 15 (2007).
 - ³ T. Dietl, J. Appl. Phys. **103**, 07D111 (2008).
 - ⁴ A. Bonanni and T. Dietl, Chem. Soc. Rev. **39**, 528 (2010).
 - ⁵ M. Tanaka, M. Yokoyama, P. N. Hai, and S. Ohya, in *Spintronics*, edited by T. Dietl, D. D. Awschalom, M. Kaminska, and H. Ohno (Elsevier, Amsterdam, 2008), p. 455.
 - ⁶ G. Martinez-Criado, A. Somogyi, S. Ramos, J. Campo, R. Tucoulou, M. Salome, J. Susini, M. Hermann, M. Eickhoff, and M. Stutzmann, Appl. Phys. Lett. **86**, 131927 (2005).
 - ⁷ M. Jamet, A. Barski, T. Devillers, V. Poydenot, R. Dujardin, P. B. Guillemaud, J. Rothman, E. B. Amalric, A. Marty, J. Cibert, et al., Nat. Mat. **5**, 653 (2006).
 - ⁸ S. Kuroda, N. Nishizawa, K. Takita, M. Mitome, Y. Bando, K. Osuch, and T. Dietl, Nature Mat. **6**, 440 (2007).
 - ⁹ A. Bonanni, M. Kiecana, C. Simbrunner, T. Li, M. Sawicki, M. Wegscheider, M. Quast, H. Przybylinska, A. Navarro-Quezada, R. Jakiela, et al., Phys. Rev. B **75**, 125210 (2007).
 - ¹⁰ A. Bonanni, A. Navarro-Quezada, T. Li, M. Wegscheider, Z. Matěj, V. Holý, R. Lechner, G. Bauer, M. Rovezzi, F. d'Acapito, et al., Phys. Rev. Lett. **101**, 135502 (2008).
 - ¹¹ M. Rovezzi, F. d'Acapito, A. Navarro-Quezada, B. Faina, T. Li, A. Bonanni, F. Filippone, A. Bonapasta, and T. Dietl, Phys. Rev. B **79**, 195209 (2009).
 - ¹² C. Liu, F. Yun, and H. Morkoç, J. Mater. Sci.:Mater. Electron. **16**, 555 (2005).
 - ¹³ J. M. D. Coey, K. Wongsaprom, J. Alaria, and M. Venkatesan, J. Phys. D: Appl. Phys. **41**, 134012 (2008).
 - ¹⁴ J. D. Boeck, R. Oesterholt, A. V. Esch, H. Bender, G. Biliyar, C. V. Hoof, and G. Borghs, App. Phys. Lett. **68**, 2744 (1996).
 - ¹⁵ P. Nam-Hai, Naganuma, S. Ohiya, M. Tanaka, S. E. Barnes, and S. Maekawa, Nature **458**, 489 (2009).
 - ¹⁶ T. Devillers, M. Jamet, A. Barski, V. Poydenot, P. Bayle-Guillemaud, E. Bellet-Amalric, S. Cherifi, and J. Cibert, Phys. Rev. B **76**, 205306 (2007).
 - ¹⁷ T. Dietl, Nature Mat. **5**, 673 (2006).
 - ¹⁸ S. Kuwabara, T. Kondo, T. Chikyow, P. Ahmet, and H. Munekata, Jpn. J. Appl. Phys. **40**, L727 (2001).
 - ¹⁹ M. Kane, S. Gupta, W. Fenwick, N. Li, E. Park, M. Strassburg, and I. Ferguson, phys. stat. sol. (b) **204**, 61 (2007).
 - ²⁰ T. Fukushima, K. Sato, H. Katayama-Yoshida, and P. Dederichs, Jpn. J. Appl. Phys. **45**, L416 (2006).
 - ²¹ C. Simbrunner, M. Wegscheider, M. Quast, T. Li, A. Navarro-Quezada, H. Sitter, A. Bonanni, and R. Jakiela, Appl. Phys. Lett. **90**, 142108 (2007).
 - ²² F. d'Acapito, S. Colonna, S. Pascarelli, G. Antonioli, A. Balerna, A. Bazzini, F. Boscherini, F. Campolungo, G. Chini, G. Dalba, et al., ESRF Newsletter **30**, 42 (1998).
 - ²³ D. Rechenbach and H. Jacobs, J. Alloys Compds. **235**, 15 (1996).
 - ²⁴ H. Jacobs, D. Rechenbach, and U. Zachwieja, J. Alloys Compds. **227**, 10 (1995).
 - ²⁵ H. Swanson and E. Tatge, National Bureau of Standards **539**, 1 (1955).
 - ²⁶ A. Gorton, G. Bitsianes, and T. Joseph, Transactions of the Metallurgical Society of Aime (1965).
 - ²⁷ Y. Joly, O. Bunafu, J. Lorenzo, R. Galéra, S. Grenier, and B. Thompson, J. Phys: Conf. Series **190**, 012007 (2009).
 - ²⁸ A. Ankudinov, B. Ravel, J. Rehr, and S. Conradson, Phys. Rev. B (1998).
 - ²⁹ B. Ravel and M. Newville, J. Synchr. Rad. p. 537 (2005).
 - ³⁰ M. Newville, J. Synchr. Rad. **8**, 322 (2001).

- ³¹ K. Klementev, J. Phys. D: Appl. Phys. **34**, 209 (2001).
- ³² W. Stefanowicz, D. Sztenkiel, B. Faina, A. Grois, M. Rovezzi, T. Devillers, A. Navarro-Quezada, T. Li, R. Jakiela, M. Sawicki, et al., *cond.-mat/0912.4216*.
- ³³ W. Pacuski, P. Kossacki, D. Ferrand, A. Golnik, J. Cibert, M. Wegscheider, A. Navarro-Quezada, A. Bonanni, M. Kiecana, M. Sawicki, et al., Phys. Rev. Lett. **100**, 037204 (2008).
- ³⁴ K. H. Jack, Acta Cryst. **5**, 404 (1952).
- ³⁵ R. T. Lechner, V. Holý, S. Ahlers, D. Bougeard, J. Stangl, A. Trampert, A. Navarro-Quezada, and G. Bauer, Appl. Phys. Lett. **95**, 023102 (2009).
- ³⁶ G. Williamson and W. Hall, Acta Metall. **1**, 22 (1953).
- ³⁷ T. Li, C. Simbrunner, A. Navarro-Quezada, M. Wegscheider, M. Quast, D. Litvinov, D. Gerthsen, and A. Bonanni, J. Cryst. Growth **310**, 3294 (2008).
- ³⁸ B. Eck, R. Dronskowski, M. Takahashi, and S. Kikkawa, J. Mat. Chem. **9**, 1527 (1999).
- ³⁹ © *international centre for diffraction data. all rights reserved* (2009).
- ⁴⁰ A. Leineweber, H. Jacobs, F. Hüning, H. Luecken, H. Schilder, and W. Kockelmann, J. Alloys Compds. **288**, 79 (1999).
- ⁴¹ D. Keavney, D. Storm, J. Freehand, I. Grigorov, and J. Walker, Phys. Rev. Lett. **74**, 4531 (1995).
- ⁴² Z. Shi, J. Cooke, Z. Zhang, and B. Klein, Phys. Rev. B. **54**, 3030 (1996).
- ⁴³ E. Malguth, A. Hoffmann, and M. R. Phillips, phys. stat. sol. (b) **245**, 455 (2008).
- ⁴⁴ R. Bouchard, C. Frederick, and V. Johnson, J. Appl. Phys. **45**, 4067 (1974).
- ⁴⁵ T. Hinomura and S. Nasu, Nouvo Cimento **18**, 253 (1996).
- ⁴⁶ H. Naganuma, Y. Endo, R. Nakatani, Y. Kawamura, and M. Yamamoto, Sci. Technol. Adv. Mater. **5**, 83 (2004).